Structural changes of thermal sprayed graphene nano platelets film into amorphous carbon under sliding wear

K. Derelizade[a], F. Venturi[a], R.G. Wellman[b], A. Khlobystov[c], T. Hussain[a],*

[a] *Faculty of Engineering, University of Nottingham, University Park, Nottingham NG7 2RD, United Kingdom*
[b] *Surface Engineering, Rolls-Royce plc, Derby DE24 8BJ, United Kingdom*
[c] *School of Chemistry, University of Nottingham, University Park, Nottingham NG7 2RD, United Kingdom*

ARTICLE INFO

ABSTRACT

Graphene has become a promising candidate to protect surfaces against friction due to its strength and lubricating ability. In this study, graphene nano platelets (GNP) thin films have been deposited onto stainless steel substrates by axially injecting GNP suspension through high velocity oxy fuel thermal spray gun. The tribological performance of the films under dry sliding wear was investigated through unlubricated ball on disc sliding wear test against a sintered alumina counter body ball under 5 N load. The understanding of the behaviour of the GNPs under sliding wear will be useful for improving the performance of graphene-based coatings which are in demand for wear resistant applications. A film was deposited showing significant improvements in friction with coefficient of friction value reduced by 7 times compared to uncoated stainless steel, even for a discontinuous film. A morphological analysis shows sliding wear led to change in particle shape from angular flakes into randomly oriented circles. Interatomic bonding and structural analysis performed reveals oxidation defect formations during wear test. Structural degradation and oxidation of GNPs during the process led to formation of amorphous carbon from graphene. Amorphous carbon formation reduces the lubricating ability and strength of the film, leading to failure.

1. Introduction

Graphene is an allotrope of carbon characterized by a 2D network of sp^2 hybridised carbon atoms bonded to each other in a hexagonal lattice. Graphene is also the basic structural unit of carbon nanotubes (CNT), graphite and fullerenes. From chemistry point of view, the term graphene is used to refer to a single layer only and particles with more than one layer are known as graphite. However, many researchers use graphene containing names such as graphene nano-platelets (GNPs) or multilayer graphene (MLG) to define a few layers (usually up to 20) of graphene according to the convention in their respective field. Stacks of more than more than 20 layers are usually referred to as thick graphene sheets [1]. Graphene is known as the strongest material discovered so far and that is why it attracted the interest of surface engineers. Studies performed on elastic properties and intrinsic strength of pristine graphene via atomistic simulations and atomic force microscopy (AFM) showed that the in plane Young's modulus is ≈ 1 TPa and the tensile strength value is higher than 100 GPa [2–4]. Depending on the production method of graphene, it can be polycrystalline and have grain boundaries which might lead to weakness compared to pristine

graphene. A study performed on chemical vapour deposition (CVD) grown graphene shows that the elastic stiffness is the same as pristine graphene and strength is only reduced by approximately 20 GPa [5]. Also, graphene has good thermal conductivity and electrical conductivity. Molecular dynamic simulations, Raman spectroscopy and thermal conductivity measurements performed on graphene in different studies led to a broad range of values from 1000 to 5000 W/mK [6–8]. Assumptions about the absorbance of graphene and dimension of the samples used during the studies are the main factors that yield this broad range of values. The electrical conductivity of graphene also depends on the shape of samples tested and the packing density. According to studies performed on graphene compacted into various shapes and with different pressure electrical conductivity varies from ≈ 100 S/m to ≈ 1000 S/m [9,10]. In addition, graphene has lubrication ability, enhanced surface properties and chemical inertness due to its low reactivity once dangling bonds are passivated. Outstanding properties of GNPs mentioned above made them a promising reinforcement material for composite manufacturing. After their discovery, GNPs have been added to metal, ceramic, cermet (metal & ceramic) and polymer matrices via various manufacturing methods to improve the mechanical

---

* Corresponding author.
  E-mail address: Tanvir.Hussain@nottingham.ac.uk (T. Hussain).

properties of the matrix material. Hardness, yield strength and ultimate tensile strength are a few of the improved mechanical properties reported due to the addition of GNPs. Range of improvements in mechanical properties are varied form 20% to even more than 100% depending on the concentration of the GNPs [11–19].

GNP strength, shearing ability and chemical inertness also give rise to enhanced wear resistance in addition to improved mechanical properties of composites. Mechanical failure due to wear and generation of friction are the most common forms of failure in moving and rotating parts. Hence, wear resistance and tribology properties have high importance for composites used in moving parts. Incorporation of GNPs into ceramic and metal matrices improve the wear resistance via combination of two different mechanisms. Improved wear performance has been linked to both improvements in fracture toughness and hardness, and formation of protective tribofilms due to the exfoliation of GNPs. A major contributor mechanism to the improved wear resistance has not been identified yet; some studies reported fracture toughness as the main contributor while other studies did not. Two different studies investigate the tribological performance of alumina / GNP composites via unlubricated ball on disc tests and wear resistance improved by two order of magnitude at 10 N load against alumina counter-body [20] and one order of magnitude at 25 N against tungsten carbide counter-body [21]. According to the first study, the main reason behind the improved wear performance is the improved localised mechanical properties and fracture toughness rather than a tribofilm formation. Silicon nitride is another ceramic which was investigated in both lubricated (isooctane) and unlubricated conditions. Wear performance of SiN / GNP composites against a silicon nitride counter-body in the presence of isooctane shows that the wear resistance was increased. It has been also reported that due to the exfoliation of GNPs a protective tribofilm was produced [22]. Wear performance of silicon nitride in unlubricated conditions also shows improvements in wear resistance by 5.5 times against an alumina counter surface and by 8.5 times against borosilicate counter surface [23]. In a study performed on wear performance of alumina / GNP composite at 40 N load against a ceramic counter-body, Archard wear equation was used to calculate the theoretical wear loss and hence wear rate. The Archard wear equation relates the volume worn per unit sliding distance to the normal load and the hardness of the softer surface [24]. Theoretical results showed a 21.7% increase in wear resistance as a result of hardness. However, experimental results showed an increase around 65% [25]. The formation of a tribofilm was also observed during the test and this is reported to be the dominant mechanism for improved wear resistance in this case. Improvements in wear resistance for the metal matrix were also obtained. Incorporation of GNPs into a magnesium matrix lead 40% and 60% reduction in depth and width of the wear track respectively compared to pure magnesium. GNP particles were pulled out during the test and acted as a solid lubricant [26].

GNP incorporated composites have been studied extensively, however, wear or tribological performance of GNP films alone have not been studied in detail, which might help to understand the mechanisms responsible for improved wear properties in composites. Atomic force microscopy (AFM) and friction force microscopy (FFM), micro tribometer and micro stracth test methods were used to investigate the tribological performance of graphene at the nano and micro scale level [27–34]. Test were performed on either single or few layers of deposited or grown graphene films for applications in electronic devices mostly and analysis was carried out in atomic scale. However, macro scale tribological performance was not investigated in detail where a bulk amount of graphene film subjected to larger loads (in Newtons, N instead of mN) over a bigger contact area than a FFM or AFM tip. There are a few studies involving graphene spread over a surface contact area, as a solid lubricant in which bonding between surface and graphene was not aimed. Although there was not any mechanical or chemical bonding between the graphene and the applied surface, results showed

promising improvements in coefficient of friction (down to around 0.2) and wear performance [35,36]. In recent studies, GNP films were deposited using a thermal spray flame to achieve a film on the surface, which again led to a reduction in coefficient of friction down to 0.1 as a result of a GNP tribofilm formation [37,38].

In this study a pure GNP film was produced by using suspension high velocity oxy fuel (S-HVOF) thermal spray technique. S-HVOF is a modified version of HVOF thermal spray which requires the use of liquid suspension feedstock instead of powder. Suspension feedstock allows the usage of nano and sub-micron sized particles to be sprayed through HVOF thermal spray system and is a promising technique to form films with tailored microstructures. HVOF thermal spray technique is widely used in industry, as it leads to the production of coatings with lower porosity, higher bonding strength and hardness in shorter period of time. It is a fast and effective method to deposit GNPs over extended surfaces. Potential usage of the deposited film as a protective layer against wear is discussed by analysing sliding wear test results and structural changes of graphene throughout the test. Once all the mechanisms responsible for failure and the main reason for improved tribological performance are understood, GNPs can be engineered to improve the service life or performance of GNP films and GNP incorporated composites.

2. Experimental

2.1. Feedstock preparation

GNP suspension in deionised water was prepared using 1 wt% GNPs (product no. AB 304022, ABCR, Germany) which have 6–8 nm nominal thickness and 5 μm average lateral size. Fig. 1 shows the morphology of the GNP particles used in this study. Sodium dodecyl sulphate, SDS (product no. 71725, Sigma –Aldrich, United Kingdom) was added as a surfactant to promote dispersion of GNPs. The amount of surfactant added was 1 wt% of the GNPs used. The prepared suspension was stirred by using a FB-505 Ultrasonic Processor (Fischer scientific, United Kingdom) which operates at 20 kHz with two seconds pulse every five seconds for one hour.

2.2. Substrate surface preparation

AISI 304 stainless steel (SS) substrates with nominal composition of Fe-19.0Cr-9.3Ni-0.05C (all in wt. %) were used, which have dimensions of 60 × 25 × 2 mm. Substrates were grinded by using sequential silicon carbide (SiC) grinding pads which had grit sizes P240, P400, P800 and P1200, respectively. This surface treatment was followed by polishing, utilising diamond polishing pads of average particle diameter of 6 μm and 1 μm, respectively. Prior to spray, the substrate surfaces were cleaned with industrial methylated spirit (IMS).
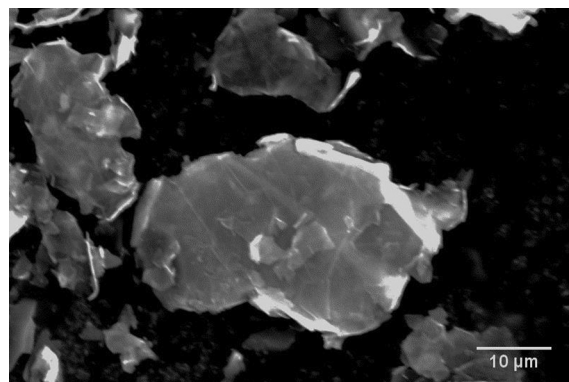
Fig. 1. SE micrograph of as - received GNP powder before forming suspension in deionised water.

2.3. Thermal spray preparation

GNPs were deposited onto the polished SS substrates by using a TopGun SS (GTV GmbH, Germany) S-HVOF thermal spray system. This suspension spray gun utilises hydrogen gas as fuel which combusts with oxygen in a 22 mm long combustion chamber. Suspension was injected axially into the combustion chamber through an injector of 1 mm diameter from a mechanically stirred reservoir by a pressurised suspension feeder. Substrates were attached to a rotating carousel with a diameter of 260 mm. The carousel rotates with a speed of 73 rpm during the spray runs which gives rise to a 1 m/s linear velocity for the attached substrates. In the meantime, the spray gun moves vertically with a traverse speed of 5 mm/s, which leads to a 4 mm overlap between tracks from subsequent passes. [39]. Four different thermal spray runs were performed to investigate the effect of spray parameters, flame power, stand-off distance and suspension flow rate on the deposition efficiency. Flow rates of suspension, oxygen and hydrogen were varied for different runs depending on the required flame power and suspension input. Flame powers were calculated from combustion calculations by using flow rates of oxygen and hydrogen gases. Each run was performed until 10 passes of the gun were completed. Compressed nitrogen gas directed to the carousel was used to prevent overheating of the samples. Here, nitrogen was chosen instead of air to minimise the possibility of oxidation of GNPs once deposited on the substrates and still hot and reactive. An overview of the runs and parameters used in each run are given in Table 1.

2.4. Wear testing

A ball on disc unlubricated rotational sliding wear test was performed by using a rotary tribometer (Ducom Instruments, The Netherlands). Microscale tribological performance of deposited films was investigated at 5 N load. 10 mm diameter circular wear tracks were created by using 6 mm diameter alumina (99.9% aluminium oxide) counter body balls (Dejay distributions, United Kingdom). The Samples rotated at 57 rpm for 30 min giving rise to 29.8 mm/s sliding linear speed and 53.7 m sliding distance.

2.5. Material characterisation

2.5.1. Scanning electron microscopes (SEM)

Surface morphology imaging of deposited coatings and worn surfaces after the tribology tests was performed by using a Quanta 600 SEM (FEI, The Netherlands) in SE mode with 10 kV accelerating voltage and 12 mm working distance. The average coverage obtained was estimated by applying threshold to SEM micrographs on imageJ (NIH, USA) software. A 7100F field emission gun scanning electron microscope (FEG–SEM) (JEOL, Japan) was used for high resolution imaging of worn areas in SE mode with 5 kV accelerating voltage and 10 mm working distance. SE mode was chosen as detected electrons originate mainly from the surface and allow a better topography analysis of the samples, especially in the case of thin GNP films.

2.5.2. Raman spectroscopy

A Jobin YVON LabRAM HR spectrometer (Horiba jobin YVON,

Japan), modified by addition of an automated xyz stage (Märzhäuser, Germany) was used to perform Raman spectroscopy. Before the spectra collection, the instrument was calibrated using a standard Si (1 0 0) reference band at 520.7 cm^{-1} and the Rayleigh line at 0 cm^{-1}. Spectra were obtained by using a red laser with wavelength of 660 nm together with 300 μm pinhole and an objective yielding 100x magnification. A 1% laser filter was applied to attenuate the intensity at the sample, as normally used to prevent damaging of carbon based samples. A 300 lines/mm rotatable diffraction grating was employed for scanning a range of Raman shifts during each acquisition. The detection of signals to create spectra was done by using a Synapse detector (Horiba, Japan). Each individual spectrum was collected for 180 s and repeated for 3 times to eliminate artefacts generated by cosmic rays and to improve signal to noise ratio. Raman spectra from 5 different points were obtained and averaged for each spectrum here reported. Spectra were corrected by applying linear baseline subtraction to eliminate fluorescence and normalised to the intensity of the characteristic carbon G band by using Labspec 6 software (Horiba jobin YVON, Japan).

2.5.3. Field emission gun – transmission electron microscopy (FEG-TEM)

As-received GNP powder and worn GNP particles (wear debris formed after the wear test mentioned at section 2.4) from the wear track was collected and suspended into propan-2-ol solution. Suspension was then transferred onto holey carbon TEM grids and left to dry. A 2100F FEG-TEM (JEOL, Japan) operated at 200 kV was used for bright field imaging for both powders. Electron energy-loss spectroscopy (EELS) was performed using an Enfinium detector (Gatan, USA) with 2 mm aperutre and an acquisition time of 0.262 s. Gatan Microscopy Suite software (GMS3) was used to analyse EELS spectra and subtract background signal. Furthermore, Fast Fourier's Transform function of the software (Live FFT) was applied to high magnification TEM micrographs to analyse the crystal structure of the sample in chosen areas.

2.5.4. Atomic force microscopy

Atomic force microscopy (AFM) measurements were performed via an Asylum Research MFP-3D (Oxford instruments ltd., UK) instrument in amplitude modulated tapping mode (AC). Scratches were made onto the GNP film / substrate surface with tweezers in order to remove GNPs from the surface and variation of height across the scratches was measured to estimate the thickness of the film.

2.5.5. Surface analysis

Alicona G5 infinite focus (Alicona imaging GmbH, Austria) instruments was used to perform surface texture measurements. Data was obtained from 161 μm × 161 μm square areas via a 100x objective lens followed by noise and tilt corrections. Surface texture measurements obtained were used to estimate the thickness of the film.

3. Results

3.1. Coating characterisation

Fig. 2 shows surface morphology of the deposited films for each run at both high and low magnification. Both angular and tiny GNP flakes

Table 1
Spray parameters used to perform each S-HVOF thermal spray run.

Spray runs	Spray parameters		
	Flame power (kW)	Stand-off distance (SoD) (mm)	GNP suspension flow rate (ml/min)
Run #1 (baseline)	25	85	70
Run #2 (Effect of flow rate)	25	85	125
Run #3 (Effect of SOD)	25	100	125
Run #4 (Effect of Flame Power)	50	100	125
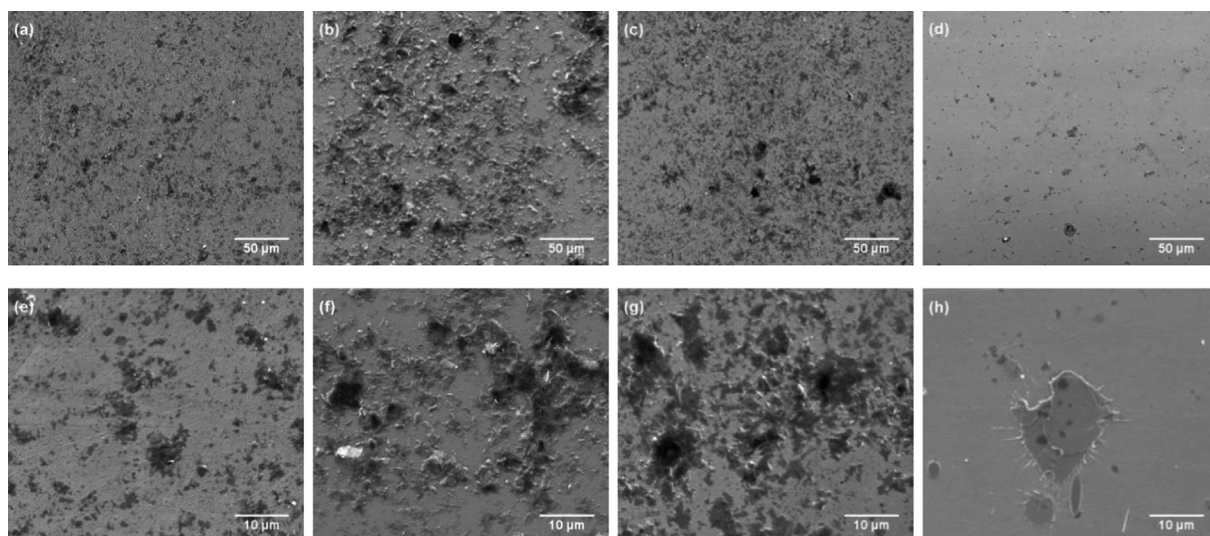
Fig. 2. Low and high magnification SE micrographs showing the surface morphology of GNP films produced by Run #1 (a,e), Run #2 (b, f), Run #3 (c, g), Run #4(d, g).

Table 2
Percentage area coverage by the deposited film for each run estimated by applying contrast threshold to SEM micrographs and measuring the area fraction via ImageJ software. The associate error is the standard error of the mean.

Samples	Area Coverage (%)
Run #1	31.5 ± 2.6
Run #2	49.5 ± 0.5
Run #3	58.0 ± 4.0
Run #4	7.0 ± 0.6

and bigger randomly shaped agglomerated GNP blocks are present on the surface. A uniform film was not achieved by any of the runs and GNP particles have a random distribution on the surface. Table 2 shows the area coverage obtained by each run, Run #1 was performed by injecting suspension at a rate of 70 ml/min into a 25 kW flame and substrates were positioned 85 mm away from the gun exit. This configuration leads to a 31.5% area coverage (as estimated from Fig. 2 a, e). The flow rate of the suspension was increased to 125 ml/min for Run #2 which gives rise to an increase in coverage by more than 50% (Fig. 2 b, f). Run #3 was performed by keeping the flow rate at 125 ml/min and increasing the stand-off distance to 100 mm. The area coverage of GNPs increased from 49.5% to 58% as a results of the increase in stand-off distance (Fig. 2 c, f). In the last run, Run #4, the effect of flame power was studied by increasing the power from 25 kW to 50 kW. The area coverage of GNPs reduced significantly compared to the other 3 runs, down to 7%. As the sample produced by Run #3 has highest area coverage, it has been chosen for wear test and further analysis with Raman spectroscopy, TEM and EELS. Thickness of this deposited film was estimated via AFM by the procedure described in section 2.5.4 is 482 ± 155 nm. Furthermore, surface texture measurements obtained from alicona were used to estimate the thickness as well. As the surface is only partially covered, height of the highest peak was assumed to be the thickest point of the film whereas the uncovered areas were considered the zero points. Thickness estimated from this method is 483 ± 160 nm. In addition average roughness of the film/substrate surface is 0.020 ± 0.004 µm.

Raman spectroscopy was performed on both as-received GNP particles and on the chosen deposited GNP films. Data was collected from five different areas for both specimens and spectra intensity averaged to form a single spectrum for each sample. Average Raman spectra
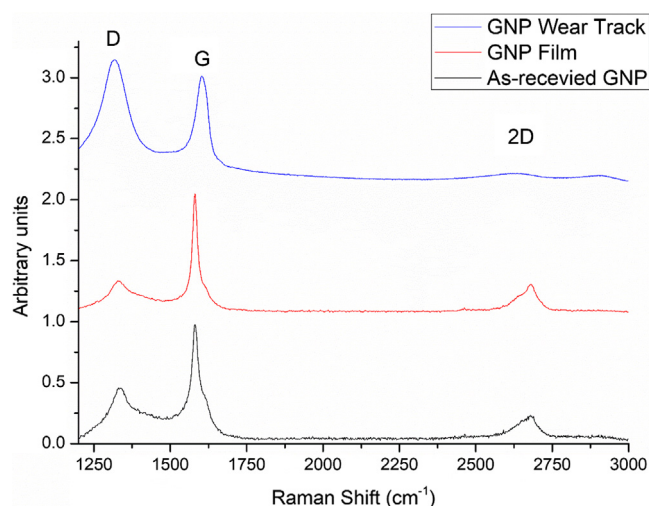
Fig. 3. Average Raman Spectra for as-received GNP, SHVOF thermal sprayed GNP film and GNP films inside the wear track obtained at 5 N Load. Spectra have been baseline corrected for fluorescence, normalised to the intensity of the G band for ease of comparison and shifted along the y-axis for clarity.

obtained exhibit three main bands showed in Fig. 3, which are fingerprints of graphitic structure. Those are the G, D and 2D bands. The G band is located at ~1580 cm^{-1}, and arises from the in plane vibrations (stretching) of sp^2 hybridized carbon–carbon bonds in hexagonal carbon rings and chains. The D band – observed at ~1350 cm^{-1} arises due to ring breathing mode (expansion / contraction) from sp^2 hybridized carbon hexagonal rings, is related to disorder and defects present in each single layer and is used to measure the amount of defects present in the hexagonal carbon ring lattice structure. The 2D band – the third characteristic band, appears at ~2700 cm^{-1}, is the second order of the D band and is related to the band structure of graphene [40,41]. Therefore, this band is related to the multi layered structure of GNPs and yields an indication of the amount of disorder between the layers. The comparison between Raman band intensity ratios (I_D/I_G and I_{2D}/I_G) was also performed and is shown in Fig. 4 to highlight the effect of the processes on the GNP structure integrity. The spectrum of the GNP film resembled the spectrum of the as-received GNPs suggesting there was minimal structural change during thermal spray. This is also proved by the consistent I_D/I_G ratios (0.39 ± 0.03
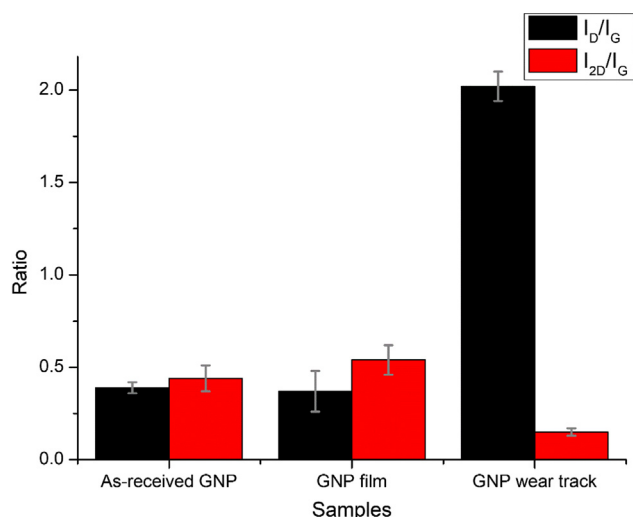
Fig. 4. Intensity ratios of Raman bands obtained for as received GNP, GNP film and GNPs inside the wear track.

and 0.37 ± 0.11 for as received GNP and GNP film, respectively). Alongside I_{2D}/I_G ratios are 0.44 ± 0.07 and 0.54 ± 0.08 representing increasing defects in the layered structure of GNPs upon thermal spray.

3.2. Tribological performance

The deposited GNP film leads to remarkable improvement in wear performance by reducing the coefficient of friction (CoF) significantly, even if a uniform film was not deposited. Fig. 5 shows CoF against cycles for a GNP deposited surface and a bare stainless steel surface for comparison. Each cycle represents one complete circular revolution (10 mm diameter) of the counter-body, and the accuracy of coefficient of friction measurements is $0.02 \pm 1\%$ measured frictional force. In the bare stainless steel case, CoF increases sharply to ~0.5 in only ~100 cycles. Then, it raises up to ~0.7 gradually with the number of cycles. In the GNP film case, the CoF remains at 0.1 up to ~875 cycles and then sharply increases to 0.5 in a few cycles. Afterwards, it follows the trend as the no film scenario by gradually increasing with the number of cycles. Repeated wear tests show the same trend. The only slight difference obtained is at the transition point, where the coefficient of friction increases from 0.1 to 0.7. This point slightly shifts earlier or later in cycles depending on the amount of GNPs present at the contact point.
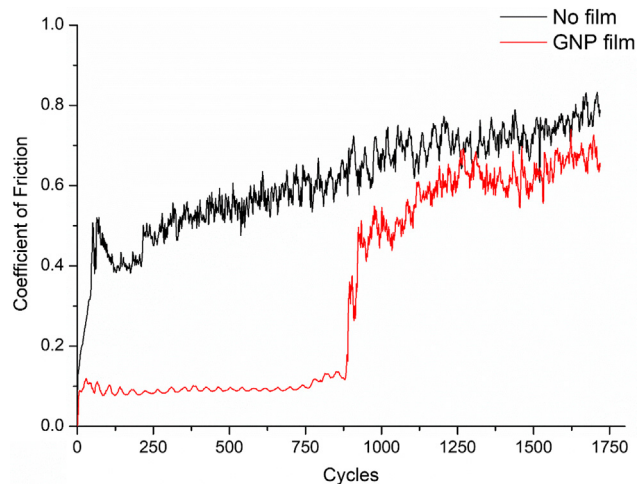
Fig. 5. Coefficients of friction against cycles for GNP film sample and a bare stainless steel substrates.

3.3. Worn surface characterisation

The worn surfaces were characterised by SEM, TEM, Raman and EELS to study the wear mechanism and deformation of the deposited film. Fig. 6 shows low magnification micrographs of wear tracks when CoF is ~0.1 (a) after ~500 cycles and ~0.7 (b) after 1700 cycles. When CoF is ~0.1, a two-body abrasive wear mechanism takes place. There is no significant damage or material removal (mild wear regime) from the substrate surface; material was shifted to the edges of the wear track indicating ploughing wear mechanism and abrasive grooves are also present. The wear track width is ~185 μm and the surface is relatively smooth. When the CoF is 0.7, the wear track is ~7 times wider and the surface is rougher. Severe damage happened to the surface, wear debris was produced and wear grooves due to material removal can be seen. This is a clear indication that the film is no longer present on the surface and a severe wear regime took place. Removal of material leads to a change of wear mechanism from two body abrasive wear to three body abrasive wear. Fig. 7 shows high magnification FEG-SEM micrographs of wear tracks when CoF is ~0.1 (a) after ~500 cycles and ~0.7 (b) after 1700 cycles. Alignment of GNPs in the direction of motion and tribofilm formation can be seen when CoF is ~0.1. When CoF is ~0.7, tribofilm is no longer present inside the wear tracks. Agglomerated chunks of GNPs got stuck inside the wear grooves or were trapped between the wear debris produced. Delamination of the surface due to severe wear regime was followed by fragmentation and led to the formation of wear debris flakes. Further analyses by TEM, Raman and EELS were performed on the wear track for CoF ~0.1, the high roughness of the wear track for CoF 0.7 prevents the calibration and usage of Raman spectroscopy. The produced films were destroyed and removed from the wear track at the stage when CoF is 0.7 therefore TEM and EELS could not be performed.

Raman spectra from five different points were obtained for GNP films inside the wear track after ~500 cycles, when the CoF was ~0.1. The spectra were averaged into a single spectrum which this time is dominated by 2 bands the G and D bands, as shown Fig. 3. The intensity of the D band increased sharply, while broadening and slight shifting of the G band occurs. I_D/I_G ratio for GNPs inside wear track is 2.02 ± 0.08, which is five times higher than the as received and deposited GNPs, suggesting that a significant amount of structural defects was introduced. The 2D band decreased significantly as can also be seen from the I_{2D}/I_G ratio (0.15 ± 0.02), that indicates a disordering of the layered structure of GNPs.

Fig. 8 shows TEM micrographs of as-received GNPs (a) and GNPs collected from the wear track after ~500 cycles (CoF ~0.1). Initially, GNP particles were angular and wide flakes were present in the as-received condition. After ~500 cycles they turned into round, irregularly shaped narrow particles. In addition, GNP particles were thinner before the application of load and turned into thicker particles, which explains the contrast difference in TEM micrographs. High magnification TEM micrographs of two different areas from GNP films inside the wear track after of ~500 cycles with diffraction patterns obtained from the marked areas are presented in Fig. 9. FFTs are used to comment on the crystal lattice structure of the particles on those specific areas. In one of the areas, angular edges completely transformed into rounded edges (Fig. 9 (a)). The FFT obtained from this area shows a ring pattern which corresponds to amorphous carbon. On the other hand, individual GNP flakes with angular edges can be seen in the second area of interest (Fig. 9 (b)). The FFT obtained from this area has both a ring and a hexagonal pattern showing that crystal lattice structure of the GNPs conserved so far, with smaller presence of amorphous carbon. After ~500 cycles, not all of the GNPs have deformed as CoF remains at ~0.1 and the presence of undeformed ones survive until ~875 cycles are reached (when CoF reaches ~0.7).

EELS spectra for as-received GNPs and GNPs collected from the wear track after ~500 cycles (CoF ~0.1) are shown in Fig. 10. The EELS spectrum of as-received GNPs resemble a graphite EELS spectrum as
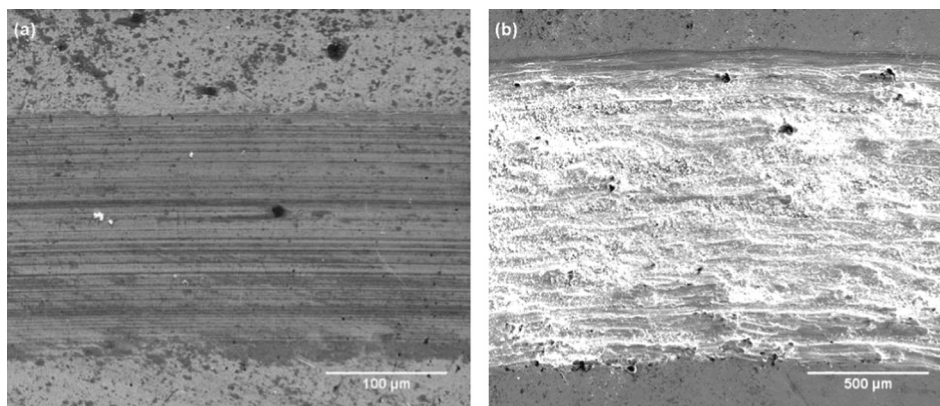
Fig. 6. Low magnification SEM SE micrographs showing the surface morphology of the wear tracks when CoF is around 0.1 (a) and 0.7 (b).
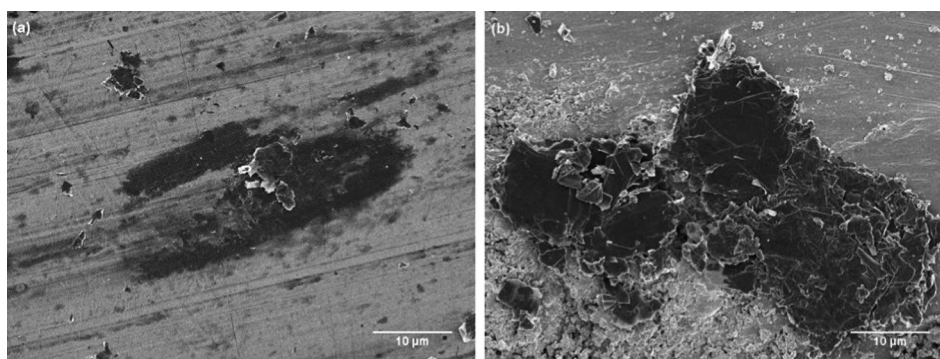
Fig. 7. High magnification FEG-SEM SE micrographs showing the surface morphology of the GNP particles inside the wear tracks when CoF is around 0.1 (a) and 0.7 (b). Tribofilm formation is shown in (a) as dark grey patches generated by GNPs exfoliated upon wear testing.

given in literature [42]. A broad band representing sigma (σ) bonding at ~300 eV loss followed by a shoulder is present. The band present at ~284 eV corresponds to pi (π) bonding [43]. The sigma bond is the bonding between sp^2 hybridized orbitals, while the pi bond is the bonding between unhybridized p orbitals in graphene [44]. On the other hand, the EELS spectrum of deformed GNPs is similar to the spectrum of amorphous carbon with an oxygen peak appearing at ~540 eV [42]. The band representing the pi bonding is un-distinguishable, and the sigma bond band is getting narrower while the shoulder disappears.

4. Discussion

4.1. Film deposition & transformation of GNPs in flame

From the material characterisation, it was clear that GNPs had random distribution and orientation on the surface. Some degree of melting of feedstock material is key for the formation of a strong bond

between the coating and substrate [45]; however, GNPs fully oxidise and combust at 600 °C before any form of melting can take place [46,47]. This prevents the formation of a strong bond with the substrate and as the process continues loosely bonded particles are removed from the surface due to the high gas velocity. Significant reduction in the GNP amount inside the wear tracks also indicates the presence of weak bonding between the coating and the substrate surface as the loosely bonded GNPs were removed due to the load exerted by the counter-body. Spray parameters used during the deposition have influence on the area coverage of the film. Instead, suspension flow rate and flame power have a major effect on coverage. Increasing flow rate leads to a higher area coverage as a result of increased number of particles sprayed per unit time. Conversely, the flame power increase has an adverse effect on deposition, leading to less than 10% area coverage at 50 kW. Higher temperature and velocity at 50 kW compared to 25 kW, lead to more combustion and removal of GNPs from the surface. The stand-off distance has a minor effect on the area coverage, only leading to less than 10% increase. The GNP deposited on substrates that are
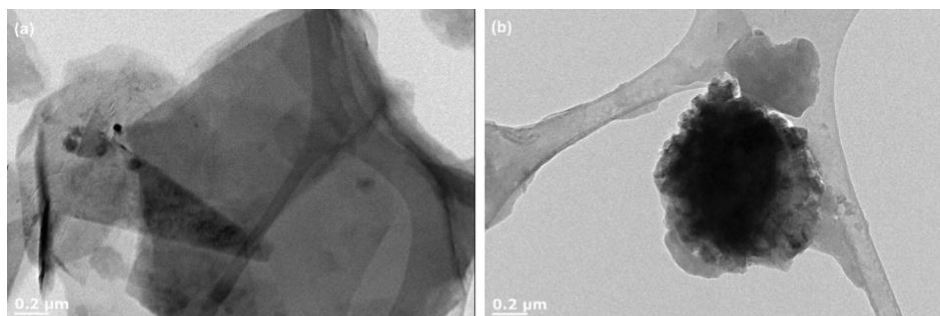
Fig. 8. TEM Micrographs of unprocessed GNPs (a) and GNPs after wear tests of 5 N while CoF is 0.1 (b).
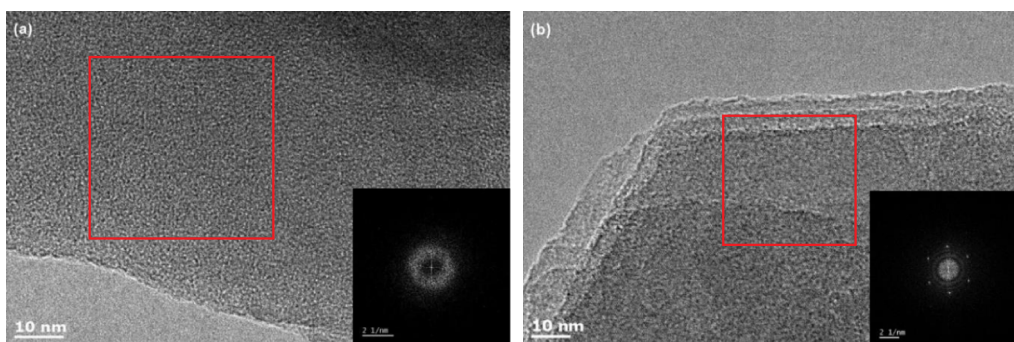
Fig. 9. High magnification TEM micrographs of GNPs after wear test and FFTs of the marked areas obtained by Gatan GMS 3 software.
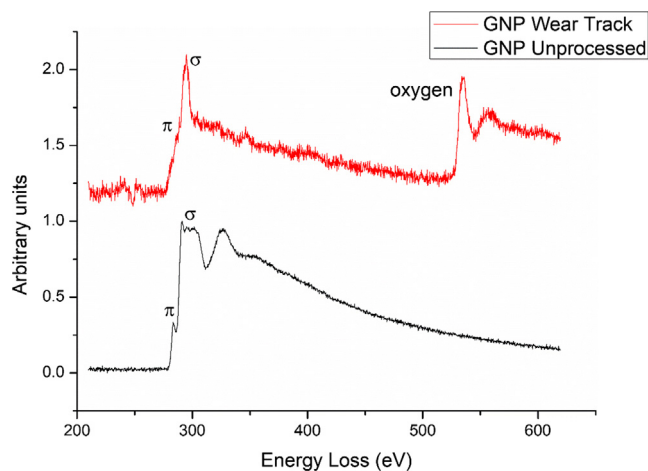
Fig. 10. EELS Spectra of the unprocessed GNPs and spectra from the wear track of the 5 N when CoF is 0.1. Spectra heave been baseline corrected for background signal, normalised to the intensity of the highest peak for ease of comparison and shifted on the y-axis for clarity.

further away from the flame are protected more against removal due to high gas velocities. However, stand-off distance cannot be increased significantly as the particles would lose their momentum before reaching the substrate. In similar studies performed via radially injecting the GNP suspension into the thermal spray flame instead of axially into the combustion chamber, led to better deposition efficiency (92% coverage) [37,38]. Radial injection reduces the degradation of GNPs inside the flame as they are subjected to the heat for a reduced amount of time. In addition higher suspension flow rate (170 ml/min) and larger standoff distance (300 mm) were used. In our study, it has been seen that increasing both flow rate and standoff distance increases the area coverage. However, the radial injection doesn't allow the full exploitation of the thrust from the thermal spray flame. Also, a too long stand-off distance could lead to a reduction of the particles velocity and raise problems of gas turbulence. These effects would ultimately lead to a poorer bonding with the substrate.

Raman spectra obtained from as-sprayed regions have all three characteristic bands (D, G and 2D) of graphene which confirms the survival of GNPs throughout the suspension preparation and thermal spray. Both suspension preparation and thermal spray processes did not induce significant defects into the graphene (no change in I_D/I_G) and did not lead to a change in the layered structure (no change in I_{2D}/I_G). Small differences in both I_D/I_G and I_{2D}/I_G ratios for as–received GNP and GNP films can be explained by inhomogeneity of GNP particles. Another study performed using the same equipment for GNP suspension preparation followed by GNP incorporation in ceramic nanocomposite coatings produced by S-HVOF thermal spray also confirmed the survival of GNPs [20].

4.2. Structural changes in GNPs during wear

Although a thick and uniform film was not achieved, conservation of the structure of GNPs during S-HVOF thermal spray leads to promising improvement in coefficient of friction during the unlubricated sliding wear tests. Layers of GNPs slid over each other when the load was applied, due to the presence of weak van der Waals bonds between the layers. Layers positioned themselves next to each other in the direction of motion and formed tribofilms, as observed inside the wear track, [25]. The tribofilm formation provides optimal wear performance even if the initial coverage was not 100%. In addition, loosely bonded GNPs transferred onto the counter-body surface. Both tribofilm formation and transfer of GNP film from the substrate to counter-body surface contributed to the low CoF values. The presence of polishing lines inside the wear track and the low CoF values indicate the surface was protected. Coefficient of friction values in between 0.1 and 0.2 were also observed in some studies where graphene was used as a solid lubricant between stainless steel bodies [34–36]. Generation of heat due to the contact pressure between the two surfaces led the film to fail after passing through a transition stage, which led to a sudden increase in CoF from ~0.1 to ~0.7. This pattern in dry air only was observed in study [36], where solution processed graphene was used as lubricant and lasted less than 100 cycles. However, constant addition of graphene usually prevents this failure but it is not possible in all applications. Deposited GNP film in our study outperformed the solution processed graphene lubricant layer even at higher sliding speed and load used to test the GNP film. The mechanism leading to failure of the film starts with the formation of oxygen bonds in between the graphene layers. Oxidation of the GNPs was confirmed by the presence of the oxygen bond peak at ~540 eV loss obtained from EELS of deformed and worn GNPs collected from wear track after ~500 cycles (CoF 0.1) [42]. The presence of oxygen bonds in between the layers changes the uniformity of the structure and introduces extrinsic defects via change of bonding type from sp^2 to sp^3 hybridization [40,48]. The change in hybridization also can be seen from the EELS spectra as the peak for pi (280 eV) bond, which corresponds to sp^2 hybridization, disappears after the wear test. Change in bonding and hybridization lead to formation of interatomic hydrogen bonding between the layers in oxidised graphene. As hydrogen bonding is a stronger interatomic bonding than van der Waals forces, layers lose their ability to slide over each other to dissipate the frictional force [34,49]. The reduction in lubrication ability causes the GNP layers to experience higher in-plane and shear stresses which induce further defects in the hexagonal structure of graphene as the wear test proceeds. In a study performed in hydrogen atmosphere in comparison to nitrogen, the wear performance of graphene improved significantly, as the hydrogen passivates the dangling carbon bonds generated by graphene rupture during wear and stabilizes the atomic shape of graphene [35]. These phenomena also prove the formation of oxygen bonds and deformation of the unique structure of graphene in air atmosphere. This phenomenon explains the sharp increase of the D band and disappearance of the 2D band, which is the characteristic band for
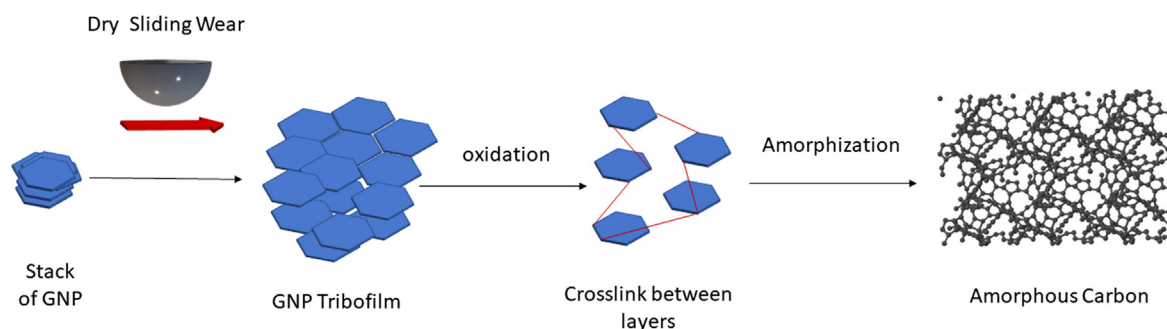
Fig. 11. Schematic diagram showing the formation of amorphous carbon from GNPs under dry sliding wear.

graphitic structures, when comparing Raman spectrum of the worn GNPs to the Raman spectra of both as-sprayed and as-received GNPs. In addition, broadening of the Raman bands after wear test and formation of a D + G peak illustrates the increase in disorder of the GNPs [41]. The loss of order in the crystal structure, therefore of crystallinity, can also be seen from change in morphology during the wear test which lead to formation of irregular spheres from cornered flakes. Once the defects reach a significant amount to deform the structure of graphene, amorphisation of GNP particles occurs and also amorphous carbon in the EELS spectrum and amorphous ring patterns in the FFT appear. Fig. 11 shows schematic diagram explaining the formation mechanism of amorphous carbon from GNPs under sliding wear.

5. Conclusion

A GNP film was deposited for the first time by axially injecting GNP suspension through a high velocity oxy-fuel thermal spray system. This is a quick and efficient method of depositing GNP films over an extended surface. A uniform film was not achieved due to weak bonding between the substrate and the film and removal of loosely bonded particles from the surface by incoming high velocity gas jet. However, significant improvements in CoF (decrease from 0.7 to 0.1) and unlubricated sliding wear (protection of the substrate) performance was observed due to tribofilm formation and lubricating ability of GNPs. The produced film acted to a greater extent like a solid lubricant during the tribological analysis. The film protected the surface up to 750 cycles under a load of 5 N. A mechanism for amorphous carbon formation from graphene under sliding wear was observed. Generation of heat as a result of friction led to oxidation of GNP films and oxygen bonds formed in between the layers. The presence of those bonds changed the bonding type and reduced the lubrication ability of the film. Once those changes reach a critical level which is enough to cause the hexagonal structure of the graphene to change into amorphous carbon, the film fails.

Findings of this study suggest bonding between the substrate and the film, the thickness and the area coverage of the films do not have a significant impact on the lubrication. However, oxidation of the GNPs during the process and deformational of hexagonal structure is critical. Therefore, if the oxidation during the wear and deformation of the structure can be prevented or delayed in a GNP containing composite coating or a film, operational lifetime and the performance of the films can be improved.

Author contributions

K.D., T.H., and A.K. conceived the idea; K.D. performed the experiment; K.D. analysed the data and F.V. analysed the EELS and TEM data; K.D. with the help from F.V. wrote the manuscript. A.K., T.H. and R.W. performed the supervision, review and editing. R.W. supplied the funding for the study. All authors discussed the results and contributed to the text of the manuscript.

Declaration of Competing Interest

The authors declare that they have no known competing financial interests or personal relationships that could have appeared to influence the work reported in this paper.

Acknowledgements

References

[1] W. Choi, I. Lahiri, R. Seelaboyina, Y.S. Kang, Synthesis of graphene and its applications: a review, Crit. Rev. Solid State Mater. Sci. 35 (2010) 52–71, https://doi.org/10.1080/10408430903505036.

[2] C. Lee, X. Wei, J.W. Kysar, J. Hone, Measurement of the elastic properties and intrinsic strength of monolayer graphene, Science 321 (2008) 385–388, https://doi.org/10.1126/science.1157996.

[3] A. Sakhaee-Pour, Elastic properties of single-layered graphene sheet, Solid State Commun. 149 (2009) 91–95, https://doi.org/10.1016/j.ssc.2008.09.050.

[4] A. Nieto, A. Bisht, D. Lahiri, C. Zhang, A. Agarwal, Graphene reinforced metal and ceramic matrix composites: a review, Int. Mater. Rev. 62 (2017) 241–302, https://doi.org/10.1080/09506608.2016.1219481.

[5] G.-H. Lee, R.C. Cooper, S.J. An, S. Lee, A. van der Zande, N. Petrone, A.G. Hammerberg, C. Lee, B. Crawford, W. Oliver, J.W. Kysar, J. Hone, High-strength chemical-vapor-deposited graphene and grain boundaries, Science 340 (2013) 1073–1076, https://doi.org/10.1126/science.1235126.

[6] A.A. Balandin, S. Ghosh, W. Bao, I. Calizo, D. Teweldebrhan, F. Miao, C.N. Lau, Superior thermal conductivity of single-layer graphene, Nano Lett. 8 (2008) 902–907, https://doi.org/10.1021/nl0731872.

[7] C. Faugeras, B. Faugeras, M. Orlita, M. Potemski, R.R. Nair, A.K. Geim, Thermal conductivity of graphene in corbino membrane geometry, ACS Nano 4 (2010) 1889–1892, https://doi.org/10.1021/nn9016229.

[8] X. Xu, L.F.C. Pereira, Y. Wang, J. Wu, K. Zhang, X. Zhao, S. Bae, C. Tinh Bui, R. Xie, J.T.L. Thong, B.H. Hong, K.P. Loh, D. Donadio, B. Li, B. Özyilmaz, Length-dependent thermal conductivity in suspended single-layer graphene, Nat. Commun. 5 (2014) 3689, https://doi.org/10.1038/ncomms4689.

[9] A. Rani, S.-W. Nam, K.-A. Oh, M. Park, Electrical conductivity of chemically reduced graphene powders under compression, Carbon Lett. 11 (2010) 90–95, https://doi.org/10.5714/CL.2010.11.2.090.

[10] B. Marinho, M. Ghislandi, E. Tkalya, C.E. Koning, G. de With, Electrical conductivity of compacts of graphene, multi-wall carbon nanotubes, carbon black, and graphite powder, Powder Technol. 221 (2012) 351–358, https://doi.org/10.1016/j.powtec.2012.01.024.

[11] M. Rashad, F. Pan, A. Tang, M. Asif, M. Aamir, Synergetic effect of graphene nanoplatelets (GNPs) and multi-walled carbon nanotube (MW-CNTs) on mechanical properties of pure magnesium, J. Alloys Compd. 603 (2014) 111–118, https://doi.org/10.1016/j.jallcom.2014.03.038.

[12] M. Rashad, F. Pan, M. Asif, A. Tang, Powder metallurgy of Mg–1%Al–1%Sn alloy reinforced with low content of graphene nanoplatelets (GNPs), J. Ind. Eng. Chem. 20 (2014) 4250–4255, https://doi.org/10.1016/j.jiec.2014.01.028.

[13] M. Rashad, F. Pan, H. Hu, M. Asif, S. Hussain, J. She, Enhanced tensile properties of magnesium composites reinforced with graphene nanoplatelets, Mater. Sci. Eng. A. 630 (2015) 36–44, https://doi.org/10.1016/j.msea.2015.02.002.

[14] M. Rashad, F.S. Pan, M. Asif, A. Ullah, Improved mechanical properties of magnesium–graphene composites with copper–graphene hybrids, Mater. Sci. Technol. 31 (2015) 1452–1461, https://doi.org/10.1179/1743284714Y.0000000726.

[15] M. Rashad, F. Pan, A. Tang, M. Asif, J. She, J. Gou, J. Mao, H. Hu, Development of magnesium-graphene nanoplatelets composite, J. Compos. Mater. 49 (2015) 285–293, https://doi.org/10.1177/0021998313518360.

[16] M. Rashad, F. Pan, A. Tang, M. Asif, S. Hussain, J. Gou, J. Mao, Improved strength and ductility of magnesium with addition of aluminum and graphene nanoplatelets (Al + GNPs) using semi powder metallurgy method, J. Ind. Eng. Chem. 23 (2015) 243–250, https://doi.org/10.1016/j.jiec.2014.08.024.

[17] K. Wang, Y. Wang, Z. Fan, J. Yan, T. Wei, Preparation of graphene nanosheet/alumina composites by spark plasma sintering, Mater. Res. Bull. 46 (2011) 315–318, https://doi.org/10.1016/j.materresbull.2010.11.005.

[18] J. Liu, H. Yan, K. Jiang, Mechanical properties of graphene platelet-reinforced alumina ceramic composites, Ceram. Int. 39 (2013) 6215–6221, https://doi.org/10.1016/j.ceramint.2013.01.041.

[19] L.S. Walker, V.R. Marotto, M.A. Rafiee, N. Koratkar, E.L. Corral, Toughening in graphene ceramic composites, ACS Nano. 5 (2011) 3182–3190, https://doi.org/10.1021/nn200319d.

[20] J.W. Murray, G.A. Rance, F. Xu, T. Hussain, Alumina-graphene nanocomposite coatings fabricated by suspension high velocity oxy-fuel thermal spraying for ultra-low-wear, J. Eur. Ceram. Soc. 38 (2018) 1819–1828, https://doi.org/10.1016/j.jeurceramsoc.2017.10.022.

[21] H.J. Kim, S.-M. Lee, Y.-S. Oh, Y.-H. Yang, Y.S. Lim, D.H. Yoon, C. Lee, J.-Y. Kim, R.S. Ruoff, Unoxidized graphene/alumina nanocomposite: fracture- and wear-resistance effects of graphene on alumina matrix, Sci. Rep. 4 (2015) 5176, https://doi.org/10.1038/srep05176.

[22] M. Belmonte, C. Ramírez, J. González-Julián, J. Schneider, P. Miranzo, M.I. Osendi, The beneficial effect of graphene nanofillers on the tribological performance of ceramics, Carbon N. Y. 61 (2013) 431–435, https://doi.org/10.1016/j.carbon.2013.04.102.

[23] H. Porwal, P. Tatarko, R. Saggar, S. Grasso, M. Kumar Mani, I. Dlouhý, J. Dusza, M.J. Reece, Tribological properties of silica–graphene nano-platelet composites, Ceram. Int. 40 (2014) 12067–12074, https://doi.org/10.1016/j.ceramint.2014.04.046.

[24] L.M. Hutchings, Triblology, Edward Arnold, London UK, 1992.

[25] C. Zhang, A. Nieto, A. Agarwal, Ultrathin graphene tribofilm formation during wear of Al 2 O 3 –graphene composites, Nanomater. Energy 5 (2016) 1–9, https://doi.org/10.1680/jnaen.15.00027.

[26] A. Das, S.P. Harimkar, Effect of graphene nanoplate and silicon carbide nanoparticle reinforcement on mechanical and tribological properties of spark plasma sintered magnesium matrix composites, J. Mater. Sci. Technol. 30 (2014) 1059–1070, https://doi.org/10.1016/j.jmst.2014.08.002.

[27] Q. Li, C. Lee, R.W. Carpick, J. Hone, Substrate effect on thickness-dependent friction on graphene, Phys. Status Solidi Basic Res. 247 (2010) 2909–2914, https://doi.org/10.1002/pssb.201000555.

[28] Y. Peng, Z. Wang, C. Li, H. Lee, N. Lee, Y. Seo, J. Eom, S. Lee, Comparison of frictional forces on graphene and graphite Related content Topical Review Izabela Szlufarska, Michael Chandross and Robert W Carpick-Atomic force microscopy and spectroscopy Yongho Seo and Wonho Jhe-Study of nanotribological properties of multilayer graphene by calibrated atomic force microscopy Comparison of frictional forces on graphene and graphite, Nanotechnology 20 (2009) 6, https://doi.org/10.1088/0957-4484/20/32/325701.

[29] X. Feng, S. Kwon, J.Y. Park, M. Salmeron, Superlubric Sliding of Graphene Nanoflakes on Graphene, (2013). doi: 10.1021/nn305722d.

[30] T. Filleter, J.L. Mcchesney, A. Bostwick, E. Rotenberg, K. V Emtsev, T. Seyller, K. Horn, R. Bennewitz, Friction and Dissipation in Epitaxial Graphene Films, (n.d.). doi: 10.1103/PhysRevLett.102.086102.

[31] Z. Deng, A. Smolyanitsky, Q. Li, X.-Q. Feng, R.J. Cannara, Adhesion-dependent

[32] T. Filleter, R. Bennewitz, Structural and frictional properties of graphene films on SiC(0001) studied by atomic force microscopy, (n.d.). doi: 10.1103/PhysRevB.81.155412.

[33] K.-S. Kim, H.-J. Lee, C. Lee, S.-K. Lee, H. Jang, J.-H. Ahn, J.-H. Kim, H.-J. Lee, Chemical Vapor Deposition-Grown Graphene: The Thinnest Solid Lubricant, 15 (2020) 15. doi: 10.1021/nn2011865.

[34] D. Berman, A. Erdemir, A.V. Sumant, Graphene: a new emerging lubricant, Mater. Today 17 (2014) 31–42, https://doi.org/10.1016/j.mattod.2013.12.003.

[35] D. Berman, S.A. Deshmukh, S.K.R.S. Sankaranarayanan, A. Erdemir, A.V. Sumant, Extraordinary macroscale wear resistance of one atom thick graphene layer, Adv. Funct. Mater. 24 (2014) 6640–6646, https://doi.org/10.1002/adfm.201401755.

[36] D. Berman, A. Erdemir, A.V. Sumant, Few layer graphene to reduce wear and friction on sliding steel surfaces, Carbon N. Y. 54 (2013) 454–459, https://doi.org/10.1016/j.carbon.2012.11.061.

[37] F. Venturi, G.A. Rance, J. Thomas, T. Hussain, A low-friction graphene nanoplatelets film from suspension high velocity oxy-fuel thermal spray, AIP Adv. 9 (2019), https://doi.org/10.1063/1.5089021.

[38] F. Venturi, T. Hussain, Radial injection in suspension high velocity oxy-fuel (S-HVOF) thermal spray of graphene nanoplatelets for tribology, J. Therm. Spray Technol. 29 (2020) 255–269, https://doi.org/10.1007/s11666-019-00957-y.

[39] M. Bai, H. Maher, Z. Pala, T. Hussain, Microstructure and phase stability of suspension high velocity oxy-fuel sprayed yttria stabilised zirconia coatings from aqueous and ethanol based suspensions, J. Eur. Ceram. Soc. 38 (2018) 1878–1887, https://doi.org/10.1016/j.jeurceramsoc.2017.10.026.

[40] D. Mariotti, V. Švrček, A. Mathur, C. Dickinson, K. Matsubara, M. Kondo, Carbon nanotube growth activated by quantum-confined silicon nanocrystals, J. Phys. D. Appl. Phys. 46 (2013) 122001, , https://doi.org/10.1088/0022-3727/46/12/122001.

[41] E.I. Bîru, H. Iovu, Graphene Nanocomposites Studied by Raman Spectroscopy, in: H. I.E.-G.M. do Nascimento (Ed.), Raman Spectrosc., InTech, Rijeka, 2018: p. Ch. 9. doi: 10.5772/intechopen.73487.

[42] C. Ahn, EELS atlas : a reference collection of electron energy loss spectra covering all stable elements, Gatan Inc., Warrendale Pa., 1983.

[43] J. Xie, K. Komvopoulos, Bilayer amorphous carbon films synthesized by filtered cathodic vacuum arc deposition, J. Mater. Res. 31 (2016) 3161–3167, https://doi.org/10.1557/jmr.2016.250.

[44] W.D. Callister, D.G. Rethwisch, Materials Science and Engineering 9th Edition, 2014. doi: 10.1016/j.str.2011.03.005.

[45] L Pawlowski, The science and engineering of thermal spray coatings, 2008. https://books.google.com/books?hl=en&lr=&id=firIir6iX_AC&oi=fnd&pg=PR7&dq=the+scinece+and+enginnering+of+thermal+spray+coatings+second+ediytion&ots=GTBB3ydWRh&sig=gN9r9oF6RMgOZ2nKK0gQ0rYypkQ (accessed August 8, 2019).

[46] L. Yu, J.S. Park, Y.-S. Lim, C.S. Lee, K. Shin, H.J. Moon, C.-M. Yang, Y.S. Lee, J.H. Han, Carbon hybrid fillers composed of carbon nanotubes directly grown on graphene nanoplatelets for effective thermal conductivity in epoxy composites, Nanotechnology 24 (2013) 155604, , https://doi.org/10.1088/0957-4484/24/15/155604.

[47] S. Colonna, O. Monticelli, J. Gomez, C. Novara, G. Saracco, A. Fina, Effect of morphology and defectiveness of graphene-related materials on the electrical and thermal conductivity of their polymer nanocomposites, Polymer (Guildf). 102 (2016) 292–300, https://doi.org/10.1016/j.polymer.2016.09.032.

[48] F. Banhart, J. Kotakoski, A.V. Krasheninnikov, Structural defects in graphene, ACS Nano 5 (2011) 26–41, https://doi.org/10.1021/nn102598m.

[49] L.-F. Wang, T.-B. Ma, Y.-Z. Hu, H. Wang, Atomic-scale friction in graphene oxide: An interfacial interaction perspective from first-principles calculations, Phys. Rev. B 86 (2012) 125436, , https://doi.org/10.1103/PhysRevB.86.125436.